Research Article Vol. 31, No. 5 / 27 Feb 2023 / Optics Express 7265
Optics EXPRESS

Crystal superlattices for versatile and sensitive quantum spectroscopy

ZI S. D. TOA,[1,*] MARIA V. CHEKHOVA,[2,3] LEONID A. KRIVITSKY,[1,4] AND ANNA V. PATEROVA[1]

[1] *Institute of Materials Research and Engineering (IMRE), Agency for Science, Technology and Research (A*STAR), Singapore 138634, Singapore*
[2] *Max-Planck Institute for the Science of Light, Staudtstr. 2, Erlangen D-91058, Germany*
[3] *University of Erlangen-Nuremberg, Staudtstr. 7/B2, 91058 Erlangen, Germany*
[4] *Currently with Illumina Singapore, 29 Woodlands Industrial Park E1, Singapore 757716, Singapore*
[*] *desmond_toa@imre.a-star.edu.sg*

Abstract: Nonlinear interferometers with quantum correlated photons have been demonstrated to improve optical characterization and metrology. These interferometers can be used in gas spectroscopy, which is of particular interest for monitoring greenhouse gas emissions, breath analysis and industrial applications. Here, we show that gas spectroscopy can be further enhanced via the deployment of crystal superlattices. This is a cascaded arrangement of nonlinear crystals forming interferometers, allowing the sensitivity to scale with the number of nonlinear elements. In particular, the enhanced sensitivity is observed via the maximum intensity of interference fringes that scales with low concentration of infrared absorbers, while for high concentration the sensitivity is better in interferometric visibility measurements. Thus, a superlattice acts as a versatile gas sensor since it can operate by measuring different observables, which are relevant to practical applications. We believe that our approach offers a compelling path towards further enhancements for quantum metrology and imaging using nonlinear interferometers with correlated photons.

1. Introduction

Recent developments in quantum spectroscopy have utilized photon correlations to improve precision and accuracy and enable novel capabilities beyond traditional spectroscopy. Notable examples include using the Hong-Ou-Mandel effect to improve the measurement accuracy of material optical susceptibilities [1,2], and interferometry with frequency nondegenerate correlated photons to probe infrared (IR) properties of the material without detection of the IR photons [3–7].

The latter form of quantum spectroscopy is based upon a nonlinear interferometer utilizing nonlinear optical crystals [8–12]. In these crystals, a process known as frequency non-degenerate spontaneous parametric down-conversion (SPDC) [13–18] occurs. Here, coherent pump photons are split into quantum correlated photon pairs (or biphotons), such as a visible signal and infrared (IR) idler. These correlated photon pairs generated in different crystals can be made path- and origin-indistinguishable, resulting in interference fringes in the spectral- and angular-coordinates of signal photons, otherwise known as a λ-k spectrum [19]. It must be emphasized that this interference pattern of signal photons depends upon the combined phases and amplitudes of the pump, signal, and idler photons. Information from the interaction of IR idler photons with a sample can thus be inferred from the interference pattern of signal photons [4]. As a result, this technique bypasses difficulties in IR generation and detection via the use of visible range pump lasers and inexpensive silicon-based detectors.

Previously, carbon dioxide (CO_2) gas sensing was demonstrated via nonlinear interferometry in a Mach-Zehnder superlattice built out of a cascaded array, which we call a superlattice, of

#477019 https://doi.org/10.1364/OE.477019
Journal © 2023 Received 12 Oct 2022; revised 12 Jan 2023; accepted 12 Jan 2023; published 14 Feb 2023

Optics EXPRESS

two and five lithium niobate (LN) crystals pumped by a 532 nm wavelength continuous wave (cw) laser [20]. The five-crystals superlattice was demonstrated to be more sensitive than the two-crystals version in the measurement of CO_2 concentration [20].

However, the effects and scaling of idler absorption on the superlattice λ-k spectrum was not explored in that earlier work, as the focus was upon the fringe shifts close to the CO_2 absorption band [20]. The fringe shifts are results of refractive index changes arising from the introduction of pure CO_2 gas in the intervening gaps between the crystals in the superlattice.

In this work, we developed the theory for a lossy superlattice interferometer. We also demonstrate the advantage gained from adopting crystal superlattices in quantum spectroscopy using nonlinear interferometers while comparing with new experimental results collected along with that work [20]. We show that fringe maximum intensity displays increasing sensitivities with increasing superlattice size and increasing idler absorber concentration, while the visibility displays increasing sensitivities only at high idler absorber concentrations. Note that our definition of sensitivity is the gradient of the response of an experimental observable to concentration change in the idler absorber. As a result, a superlattice offers versatility to operate via two different measurement modes – a feature that was not reported in earlier works. Furthermore, so-called Rozhdestvenski "hooks" [21] were experimentally observed and can be simulated near the 4.3 μm CO_2 mid-IR absorption band using the Generalized Sellmeier Equation (GSE) for air [22]. Thus, our model is capable of accounting for the essential aspects of the experiment.

2. Methods

2.1. Theory

We provide a brief description of our theoretical model in this section. Detailed derivation can be found in Supporting Materials.

We begin with the simplest superlattice composed of two nonlinear crystals in a Mach-Zehnder arrangement [12] and one beamsplitter placed in the linear gap between the two crystals, see Fig. 1. This model allows us to highlight the important physics of quantum spectroscopy with the absorption of undetected idler photons. Idler absorption is modeled using the beamsplitter with real-valued idler amplitude transmission and reflection coefficients τ and r respectively. We note that our approach is similar to modelling the loss for squeezed light using beamsplitters [23].

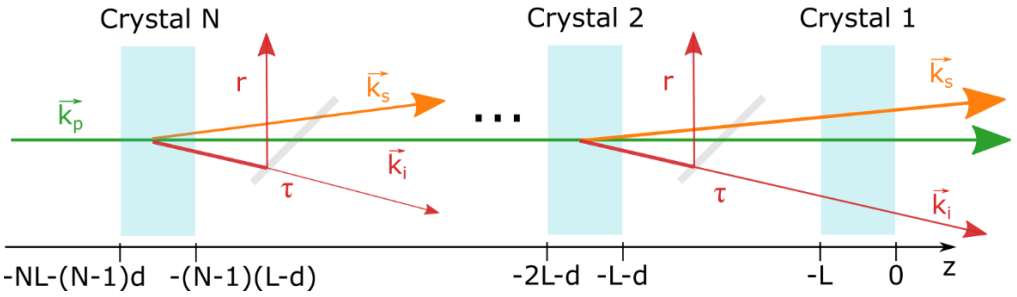

Fig. 1. Schematic of a superlattice with N crystals placed in a Mach-Zehnder arrangement. Idler absorption was modeled using a beamsplitter placed between the crystals with amplitude transmission and reflection coefficients τ and r, respectively. The coordinate origin is placed at the exit face of Crystal 1. The pump and signal photons travel without losses, and the idler experiences uniform losses throughout the gaps, a natural case for gas sensing.

In Fig. 1, the pump photons are propagating from left to right with wavevector $\vec{k_p}$. The final exit face in the superlattice is denoted as having a position of $z = 0$. As a result, the entrance face of the first crystal (from the position of $z = 0$) is at a position of $z = -L$. A linear gap of length

Optics EXPRESS

d and a beamsplitter of idler amplitude transmission coefficient τ and reflection coefficient r separates the two identical crystals. Considering a natural case for gas sensing, we shall assume here that (1) there are no losses / reflections for the pump and signal, and (2) uniform losses for the idler. The exit and entrance faces of the second crystal are thus at positions $z = -L - d$ and $z = -2L - d$ respectively.

In frequency non-degenerate SPDC, there is a small probability for each pump photon to be split into a visible signal photon and an IR idler photon with wavevectors $\overrightarrow{k_s}$ and $\overrightarrow{k_i}$, respectively. Denoting the longitudinal wavevector mismatch as $\Delta = k_s + k_i - k_p$, where k_p, k_s and k_i are, respectively, the longitudinal wavevectors of the pump, signal, and idler in the nonlinear crystal, one can write the state after Crystal 2 in Fig. 1 as:

$$|\psi\rangle_2 \sim L\, sinc\left(\frac{\Delta L}{2}\right) e^{\frac{i\Delta L}{2}} \hat{a}_s^+(-L-d)\hat{a}_i^+(-L-d)|0\rangle, \tag{1}$$

where $\hat{a}_s^+(-L-d)$ and $\hat{a}_i^+(-L-d)$ are the signal and idler photon creation operators at $z = -L-d$, respectively, and $|0\rangle$ is the vacuum state. The state after Crystal 1 in Fig. 1 is:

$$|\psi\rangle_1 \sim e^{ik_pL+ik_p'd} L\, sinc\left(\frac{\Delta L}{2}\right) e^{\frac{i\Delta L}{2}} \hat{a}_s^+(0)\hat{a}_i^+(0)|0\rangle, \tag{2}$$

where k_p' denotes the longitudinal wavevector of the pump in the gap. The influence of the beamsplitter is accounted for in the following way: $\hat{a}_s^+(-L-d) = e^{-ik_sL-ik_s'd}\hat{a}_s^+(0)$, $\hat{a}_i^+(-L-d) = \tau e^{-ik_iL-ik_i'd}\hat{a}_i^+(0) - r\,\hat{a}_0^+$, where k_s' and k_i' respectively denote the longitudinal wavevector of the signal and idler in the gap and $\hat{a}_0^+$ is the photon creation operator at the vacuum port of the beamsplitter. Thus, by denoting $(\Delta L + \Delta' d) \equiv \varphi$ (where $\Delta' = k_s' + k_i' - k_p'$ denotes the longitudinal phase mismatch in the linear gap), $\hat{a}_s^+(0) = \hat{a}_s^+$, $\hat{a}_i^+(0) = \hat{a}_i^+$ and $-k_sL - k_s'd + k_pL + k_p'd \equiv \phi$, the total state can be written as:

$$|\psi\rangle \sim |\psi\rangle_1 + |\psi\rangle_2 \sim L\, sinc\left(\frac{\Delta L}{2}\right) e^{\frac{i\Delta L}{2}} [\tau e^{-i\varphi}\hat{a}_i^+ - re^{i\phi}\hat{a}_0^+ + \hat{a}_i^+]\hat{a}_s^+|0\rangle \tag{3}$$

The signal intensity for two crystals is thus:

$$\langle I_s\rangle = \langle\psi|\hat{a}_s^+\hat{a}_s|\psi\rangle = |1 + \tau e^{-i\varphi}|^2 + r^2 = 2(1 + \tau\cos\varphi), \tag{4}$$

For an N-crystals superlattice, the contribution of the N$^{\text{th}}$ crystal (Crystal N in Fig. 1) to the final state is:

$$\begin{aligned}|\psi_N\rangle \sim\ & [e^{-i(N-1)k_sL - i(N-1)k_s'd}\hat{a}_s^+(0)\,]\times[\,\tau^{N-1}\, e^{-i(N-1)k_iL - i(N-1)k_i'd}\hat{a}_i^+(0) - \tau^{N-2}re \\ & -i(N-2)k_iL - i(N-2)k_i'd\hat{a}_0^+ - \tau^{N-3}r\, e^{-i(N-3)k_iL - i(N-3)k_i'd}\hat{a}_1^+ - \ldots - r\hat{a}_{N-2}^+]\end{aligned}$$

where repeated influences from intervening beamsplitters are accounted for.

As a result, the total state, after summing up all the individual states contributed by the different crystals is:

$$\begin{aligned}|\psi\rangle = \sum_{n=1}^{N}|\psi_n\rangle \sim \hat{a}_s^+(0)\Bigg[&\left(\hat{a}_i^+(0)\sum_{m=0}^{N-1}\tau^m e^{im\varphi}\right) - r\hat{a}_0^+ e^{i\left((k_p-k_s)L+(k_p'-k_s')d\right)} \\ &\times\sum_{m=0}^{N-2}\tau^m e^{im(\Delta L+\Delta' d)} - r\hat{a}_1^+ e^{2i\left((k_p-k_s)L+(k_p'-k_s')d\right)}\Bigg) \\ &\times\sum_{m=0}^{N-3}\tau^m e^{im(\Delta L+\Delta' d)} - \ldots - r\hat{a}_{N-2}^+ e^{i(N-1)\left((k_p-k_s)L+(k_p'-k_s')d\right)}\Bigg]\end{aligned}$$

Optics EXPRESS

The signal intensity is thus:

$$\langle I_s \rangle = |\sum_{m=0}^{N-1} \tau^m e^{im\varphi}|^2 + r^2|\sum_{m=0}^{N-2} \tau^m e^{im\varphi}|^2 + r^2|\sum_{m=0}^{N-3} \tau^m e^{im\varphi}|^2 + \ldots + r^2. \tag{5}$$

Denoting $q \equiv \tau e^{i\varphi}$ and remembering that $\sum_{m=0}^{N-1} q^m = \frac{1-q^N}{1-q}$, the signal intensity can be expressed as follows:

$$\langle I_s \rangle = \left|\frac{1}{1-q}\right|^2 \left[\tau^2|1-q^N|^2 + r^2 \sum_{m=0}^{N} |1-q^m|^2\right] \tag{6}$$

To obtain analytical expressions for the fringe visibility, we first calculate the sum in (6), which gives:

$$\sum_{m=0}^{N} |1-q^m|^2 = N + 1 + \frac{1-\tau^{2(N+1)}}{1-\tau^2} - \frac{2 - 2\tau\cos\varphi - 2\tau^{N+1}\cos(N+1)\varphi + 2\tau^{N+2}\cos N\varphi}{1+\tau^2-2\tau\cos\varphi}$$

Thus,

$$\langle I_S \rangle = \frac{1}{1+\tau^2-2\tau\cos\varphi}\left[2 + N - \tau^2 N - 2\tau^{N+2}\cos N\varphi - \frac{2(1-\tau^2)}{1+\tau^2-2\tau\cos\varphi}\right.$$
$$\left.(1 - \tau\cos\varphi - \tau^{N+1}\cos(N+1)\varphi + \tau^{N+2}\cos N\varphi)\right]$$

With this, we can derive expressions for the minimum and maximum intensities, which will be measured in our experiment:

$$\langle I_s \rangle_{max} = \frac{1}{(1-\tau)^2}[N(1-\tau^2) - 2\tau(1-\tau^N)], \tag{7}$$

$$\langle I_s \rangle_{min} = \frac{1}{(1+\tau)^2}[N(1-\tau^2) + 2\tau(1-\tau^N)] (\text{for even N}), \tag{8a}$$

$$\langle I_s \rangle_{min} = \frac{1}{(1+\tau)^2}[N(1-\tau^2) + 2\tau(1+\tau^N)] (\text{for odd N}), \tag{8b}$$

Thus, the fringe visibility, which we will infer from the experimental data, is:

$$V_{even} = \frac{\langle I_s \rangle_{max} - \langle I_s \rangle_{min}}{\langle I_s \rangle_{max} + \langle I_s \rangle_{min}} = \frac{2\tau[N(1-\tau^2) - (1-\tau^N)(1+\tau^2)]}{N(1-\tau^2)(1+\tau^2) - 4\tau^2(1-\tau^N)} \tag{9a}$$

$$V_{odd} = \frac{\langle I_s \rangle_{max} - \langle I_s \rangle_{min}}{\langle I_s \rangle_{max} + \langle I_s \rangle_{min}} = \frac{2\tau[N(1-2\tau^2) - (1+\tau^2-4\tau^{N+1})]}{N(1-\tau^4) - 2\tau^2(2-\tau^{N-1}-\tau^{N+1})} \tag{9b}$$

Equation (9)a reduces to $V_{even} = \tau$ for $N = 2$.

Note that in the following discussions, the above theory is generalized to polychromatic SPDC, by accounting for the phase-matching conditions in the crystal superlattice across all wavelengths and scattering angles detectable by the camera. Furthermore, the amount of absorption at each wavelength is accounted for by considering the absorptive lineshape of the idler absorber.

Optics EXPRESS

2.2. Experimental setup

We outline our experimental setup detailed previously in Ref. [20] in this section. However, unlike in Ref. [20], where fringe shifts outside the absorption region were analyzed, we are studying fringe changes in the CO_2 absorption band (around 4.3 µm) here. This was made possible with the crystal superlattice tuned to have the idler wavelength overlapped with these absorption bands.

A cw 532 nm wavelength laser (60 mW, Laser Quantum) pumps a set of identical 5% magnesium oxide-doped LN (5% MgO:$LiNbO_3$) crystals cut from a single master crystal (Eksma Optics). These crystals are cut at an angle of 48.5° to the optic axis, are of length 1 mm, and are coated with broadband antireflective coatings. A gap of 8.2 mm separates the crystals, which are mounted on kinematic prism mounts (KM100PM, Thorlabs), providing 0.45° adjustment per revolution, and are clamped by adjustable clamping arms (PM3, Thorlabs).

The generation of photon pairs in each crystal occurs via type-I quasi-collinear frequency nondegenerate spontaneous parametric down-conversion. The pump photons are blocked after the superlattice using a notch filter (NF03-532E-25, Semrock) and a polarizer. Signal photons are focused onto the slit of a spectrograph (Acton SpectraPro 2300i) using a 300 mm focal length lens. The interference pattern of signal photons in wavelength-angular (λ-k) coordinates is recorded using an electron-multiplying charge-coupled device (EMCCD) camera (Andor iXon 897) at the output of the spectrograph. The camera sensor has 512×512 pixels with 16 µm pixel size. During measurements, the gain of the camera is set to 290, and the temperature of the sensor is maintained at -80°C. To achieve the same flux of signal photons between the two- and five-crystal lattices, the integration time is set to 360 s and 144 s, respectively. As a result, acquired spectrum from the two-crystal lattice is slightly noisier than the five-crystals lattice due to a corresponding increased camera exposure to ambient light. The optical noise is independently measured and accounted for during data processing.

To obtain high-visibility interference patterns, crystals in this Mach-Zehnder interferometer must be carefully aligned. This is achieved via the following three steps. One, adjustment of the crystal orientations to obtain nearly identical spectra. Two, finer alignment of the crystal optical axes to the same direction was carried out via observation of the pairwise interference fringes. Three, adjustment of the distances between crystals to be equal. Thus, we mounted each crystal on a 2D translation stage for easy insertion and removal from the interferometer. This allows us to successively observe interference from two, three and four crystals, and overlap the respective fringes. Once the crystals are aligned, we measure the interference from two and five crystals.

For the gas spectroscopy experiments, the interferometer is placed in an airtight enclosure with an input channel for 99.9% pure CO_2. Idler wavelength is set to overlap with the ~4.3 µm absorption peak. The gas concentration is controlled using a commercial CO_2 sensor (Amphenol). The experiments are conducted at an ambient temperature of 22°C.

Note that the experimental setup is highly stable, due to it being a common-path nonlinear interferometer.

2.3. Data processing

The code for the SPDC spectra simulation with idler absorption was written in Python 3.8. Simulation parameters were largely obtained from the previous work [20]. Refractive indices of air were obtained using the Generalized Sellmeier Equation (GSE) of air [22]. The IR transmittance of the CO_2 gas was obtained from the HITRAN2016 [24] database via HITRAN Application Programming Interface (HAPI) [25].

Outliers outside 10 standard deviations of a Gaussian distribution of the experimental datapoints were neglected in the analysis. These outliers were caused by dark noise spikes. Furthermore, angular cross-sections were filtered using a Savitzky-Golay filter to reduce noise and obtain the overall trend. Experimental errors were accounted for in Fig. 4 via calculation of the standard

Optics EXPRESS

deviation of the EM-CCD readouts (and assuming a normal distribution of values). This helps to account for both bright and dark noise sources. Thus, this leads to a correct estimation of the uncertainties in Fig. 4.

The maximum intensity is determined by taking the average of eight surrounding pixels of the global maximum value of the angular cross-section at a specific wavelength. As a result, the situation that a few pixels being very prone to noise was avoided, as these angular cross-sections were already slightly de-noised using the above-mentioned Savitzky-Golay filter.

3. Results and discussion

We demonstrate that the sensitivity advantage of crystal superlattices is, respectively, operative in two different concentration regimes using different experimental observables with the increasing number of constituent crystals. It is the maximum intensity (visibility) of the fringes that exhibits increasing sensitivity with increasing superlattice size at low (high) idler absorber concentrations.

3.1. Comparison between model and experimental results

We first prove the close similarity between the simulated and experimental λ-k spectra for both two and five crystals superlattices, see Fig. 2. Three observations stand out:

1. The interference fringes were sharper in the five-crystals superlattice than in the two-crystals superlattice, which we have experimentally demonstrated in [20]. Our theoretical model confirms this observation.

2. The appearance of Rozhdestvenski's "hooks" [21] around a CO_2 concentration of 30000 ppm, see Fig. 2(b), (d), (f) and h. These Rozhdestvenski "hooks" are a result of the rapid refractive index changes near IR molecular absorption bands. Thus, they were also captured by our simulation using the GSE for air, as the GSE includes the rapid refractive index changes.

3. The maximum fringe intensity decreased more rapidly with increasing CO_2 concentration for the five-crystals superlattice than for the two-crystals superlattice at low CO_2 concentrations, see also Fig. 4(b). On the other hand, as we will show later, the fringe visibility is more sensitive at high concentrations with an increasing number of constituent crystals in a superlattice.

This decrease in the maximum fringe intensity is more pronounced in Fig. 3(c) and (d), showing the experimental angular cross-sections at 0.607 μm wavelength (corresponding to an idler wavelength of 4.306 μm) for various CO_2 concentrations in the two- and five-crystals superlattices. Note that the angles plotted in this work are the experimentally observed external angles. The angular cross-sections show the more rapid decrease in maximum intensity of the fringes for the five-crystals superlattice than for the two-crystals case upon introduction of CO_2 gas. This behavior was also reproduced by our theoretical model, see Fig. 3(a) and (b), giving us confidence that we can adopt our theoretical approach to explore the behavior of these superlattices further.

It might seem surprising that increasing idler absorption can dramatically decrease the maximum intensity of the signal photon. One way to think about this is that the maximum signal intensity results from the "coherent" superposition of the SPDC two-photon (or biphoton) state vectors from the five constituent crystals [26]. This superposition is disrupted upon the introduction of idler absorbers, leading to a more rapid decrease in the maximum intensity of the fringe.

In addition, a longer crystal superlattice provides a higher flux of signal photons, which increases the signal-to-noise ratio for signal detection. The experimental signal-to-noise ratios

Optics EXPRESS

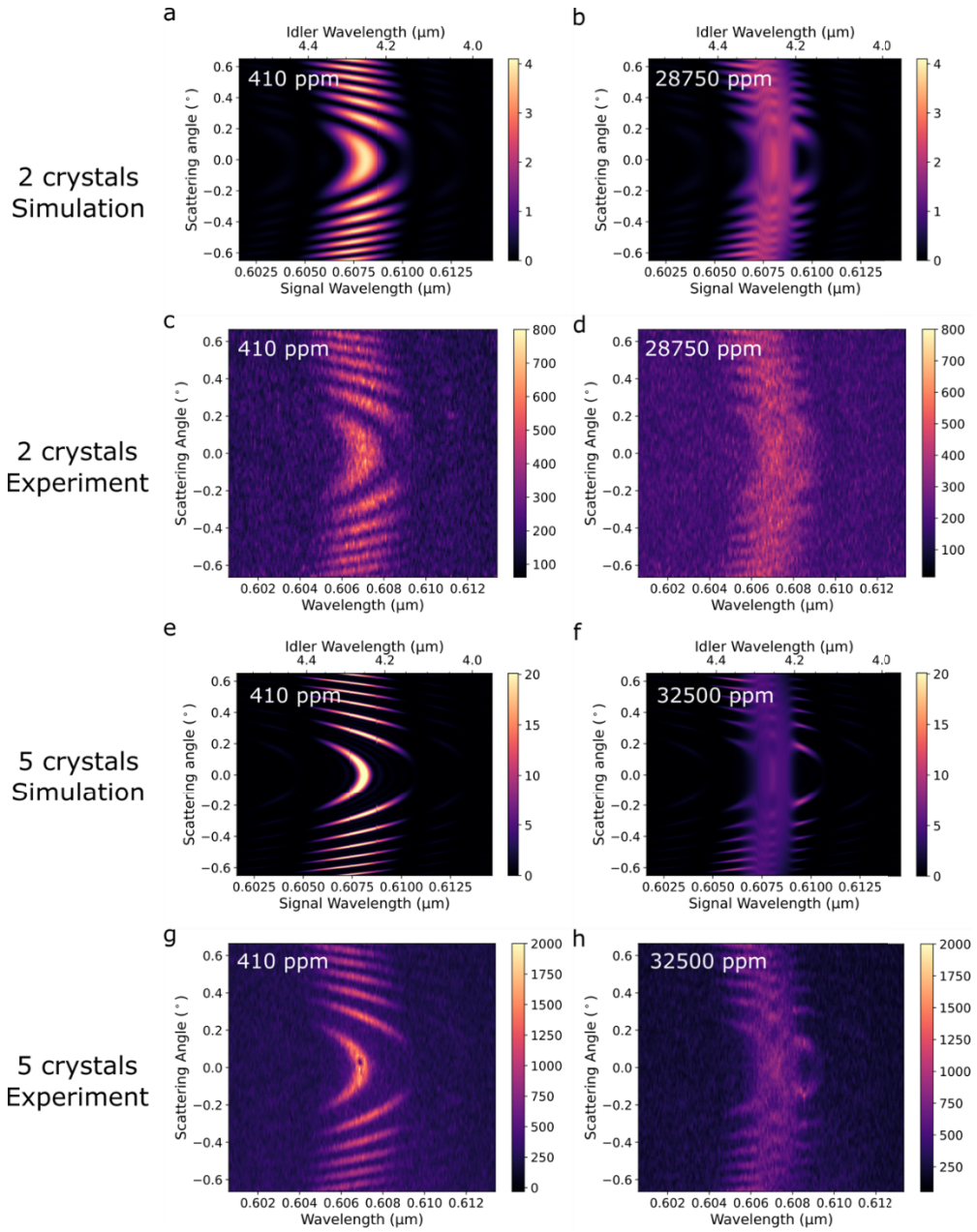

Fig. 2. Comparison of (a, b, e, f) simulated and (c, d, g, h) experimental λ-k spectra from (a-d) two and (e-h) five crystals superlattice at various CO_2 concentrations (ppm). Two different sets of CO_2 concentrations were used for the two and five crystals superlattice. Note the appearance of Rozhdestvenski's "hooks" around concentrations of 30000 ppm in both (b, f) simulated and (d, h) experimental spectra. Note, too, the more significant decrease in maximum fringe intensity for five crystals than for two crystals.

Optics EXPRESS

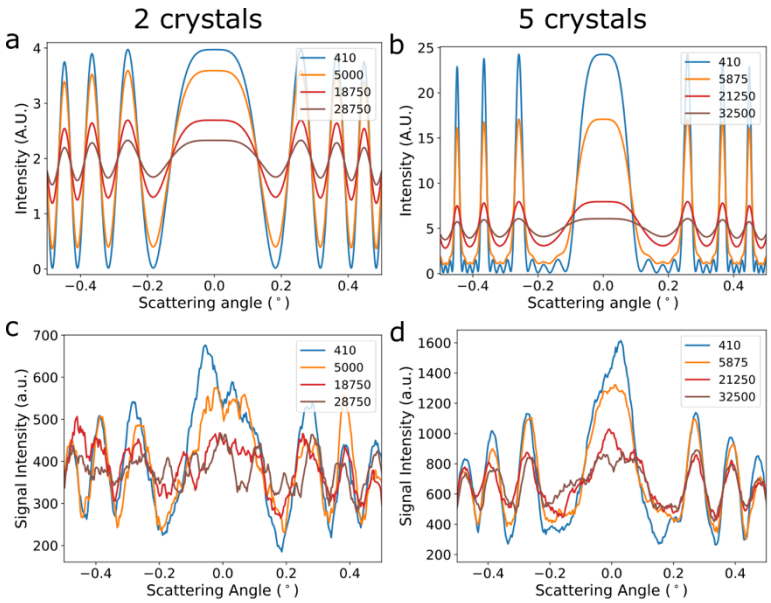

Fig. 3. (a, b) Simulated angular (external emission angle) cross-sections of SPDC spectra at a wavelength of 0.607 µm for (a) two- and (b) five-crystals superlattices for different CO_2 concentrations (in ppm). (c, d) Experimental angular cross-sections at the same wavelength of 0.607 µm for (c) two- and (d) five-crystals superlattices. Note how the increase in CO_2 concentration led to a greater relative decrease in fringe maximum intensities for the five-crystals superlattice than for the two-crystals superlattice. Note, too, the similarity between the simulated and experimental angular cross-sections, thus demonstrating that the experiments support the model. This demonstrates the higher sensitivity attainable with a greater number of crystals for gas sensing at low concentrations with fringe maximum intensity as the observable.

are 3.17 ± 0.50 and 5.96 ± 0.87 for two- and five-crystals superlattices respectively. Thus, the accompanying increase in sensitivity, arising from the deployment of longer superlattices, leads to an increase in the signal-to-noise ratio of the detected signal, despite limited down-conversion efficiency. This can be clearly seen when comparing Fig. 2(c) and (d) with Fig. 2 g and h, in which the latter two sub-figures show less noise. As a result, there is an increase in the signal-to-noise ratio in the detected signal accompanying the increase in sensitivity.

3.2. *Indication of sensitivity advantage with 10-crystals theoretical model*

Following the successful reproduction of trends in the experimental data using our theoretical model, we demonstrate this sensitivity advantage via a theoretical extension to 10 crystals, see Fig. 4(a) and (b). Here, we have normalized both the visibility and fringe maximum intensity (max $\langle I_s \rangle$) to their respective values at a CO_2 concentration of 410 ppm to see changes more clearly in these two observables.

Our simulated visibility (Eq. (9), see Fig. 4(a)) and fringe maximum intensity (max $\langle I_s \rangle$, Eq. (7), see Fig. 4(b)) have good agreement with the experimental data (to within experimental errors represented by the plotted error bars). This gives us confidence that our theoretical predictions for the 10 crystals case to be valid, and that we can solely refer to the respective simulated curves in the following discussion.

From Fig. 4(a), the visibility (Eq. (9)) for any number of constituent crystals in the superlattice does not simply linearly decrease with increasing CO_2 concentration. At CO_2 concentrations

Optics EXPRESS

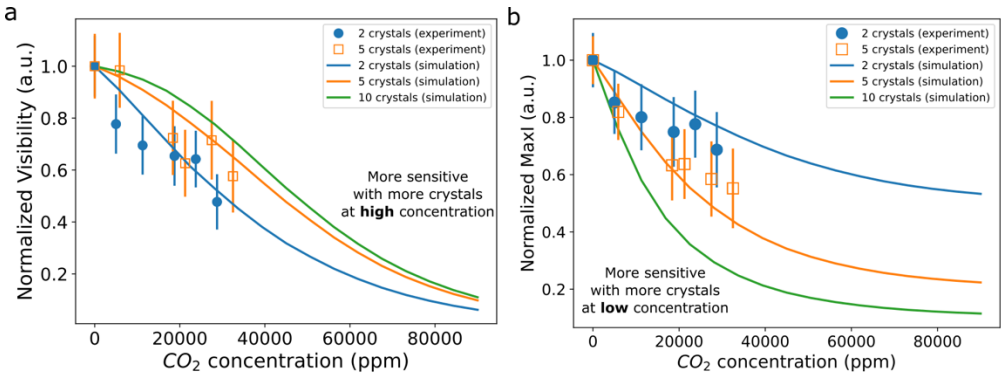

Fig. 4. Variation of the (a) simulated and experimental normalized fringe visibility (Eq. (9)) normalized fringe maximum intensity, (b) simulated and experimental normalized fringe maximum intensity (max $\langle I_s \rangle$, Eq. (7)) for different number of crystals in the superlattice with increasing gas concentration. Error bars were obtained from calculating the standard deviation of the camera readouts (assuming a normal distribution of values). The experimental values in (a) and (b) were normalized to their values at a CO_2 concentration of 410 ppm. Note that we have included simulation results using 10 crystals in (a) and (b). Unlike (b) max $\langle I_s \rangle$ which decreases more rapidly with increasing crystal superlattice size and CO_2 concentration, (a) the decrease in visibility displays non-monotonic behavior with increasing crystal superlattice size and CO_2 concentration.

higher than 30000 ppm, the visibility decreases more with both increasing number of constituent crystals in the superlattice and CO_2 concentration. This is evident from the gradient of the normalized visibility (see Fig. S1a in Supplement 1) increasing with CO_2 concentrations more than 30000 ppm for all superlattice sizes, with the gradient from the two-crystals superlattice having the least negative values at CO_2 concentrations higher than 30000 ppm. However, at CO_2 concentrations lower than 30000 ppm, the visibility decreases less rapidly with increasing CO_2 concentration with bigger crystal superlattices. Here, the gradient of the normalized visibility (see Fig. S1a in Supplement 1) decreases to a minimum around CO_2 concentration of 30000 ppm for all superlattice sizes, with the two-crystals superlattice having the most negative values at CO_2 concentrations lower than 30000 ppm. Thus, visibility sensitivity to CO_2 concentration worsens with increasing number of crystals.

On the other hand, from Fig. 4(b), max $\langle I_s \rangle$ demonstrates increasing sensitivity with increasing crystal superlattice size to increasing CO_2 concentration, regardless of the concentration regime. This can be clearly seen from the increasing negative slope of max $\langle I_s \rangle$ at CO_2 concentrations approximately less than 40000 ppm, as the number of crystals and CO_2 concentration are increased (see Fig. S1b in Supplement 1).

Thus, for quantum gas spectroscopy, a single superlattice with many constituent crystals offers versatile sensitivity advantage, as measurements can be made either using the interferometric visibility or the fringe maximum intensity. However, care must be taken in visibility measurements due to its nonlinear trend with increasing crystal superlattice size and CO_2 concentration.

In addition, looking at Fig. 4, the improvement to 10 crystals is sublinear at low CO_2 concentrations, especially for interferometric visibility. Our understanding is that, from looking at Fig. 3, the decrease in maxima fringe intensity is greater than the increase in minima fringe intensity at low CO_2 concentrations, which is expected from the disruption of quantum correlations of the SPDC biphotons state vectors. It is such a trend of decreasing contrast to a baseline not mid-way between maxima and minima (in the lossless situation) that produces a sublinear improvement, especially in visibility, to 10 crystals.

Optics EXPRESS

Note that with an estimated accuracy of 1000 ppm at low CO_2 concentrations (up to about 30000 ppm), our five-crystals superlattice is similar to a conventional CO_2 gas sensor which have an accuracy of ±10% of reading, which is about 100 ppm at low concentrations and 1000 ppm for high concentrations of CO_2 gas [27]. Even though this is still a bit of a way from NDIR CO_2 gas sensors with accuracies of ±50 ppm between 0 to 2000ppm and ± 5% of reading between 2000 to 10000 ppm [28], we note that our accuracy can be improved with more engineering and calibration. Furthermore, since the error bars have remained relatively constant, we estimate that the accuracy of our technique would not significantly deteriorate more than 1000 ppm at concentrations higher than 30000 ppm. Thus, our technique has the potential to be more accurate than NDIR sensors at high concentrations. Note, too, that we have estimated the accuracy of our superlattices from the error bars in Fig. 4 a and b.

In the other state-of-the-art work [29], an FTIR-like approach was realized, where 1% transmission accuracy was demonstrated for methane in nitrogen mixture. A total data acquisition time was 900s to achieve high SNR, accuracy, and spectral resolution. Even though our current experimental setup cannot achieve such high SNR (due to usage of bulk crystals), with a data acquisition time 10 times less, we have an estimated measurable minimum CO_2 concentration on the order of about 1000 ppm, which can be improved with larger crystal superlattices.

At this juncture, one may wonder if a 10 crystals superlattice is feasible, as fine angular and positional adjustments were required to align 5 crystals, as mentioned in the Methods, and in Ref. [20]. Indeed, the adjustment precision of the crystal angles can limit the sensitivity enhancement shown here. However, we believe that this experimental limitation can be overcome with careful future engineering/manufacturing considerations and solutions. For example, crystals could be stringently derived with the same cut angle from a master crystal. This could enable the deployment of fixed crystal holders, and cut sources of error, arising from angular adjustment, from two (crystal cut and angular mounts) to one (crystal cut). In another example, instead of building linear arrays of superlattices, one can build a superlattice with multiple passes through one crystal in a cavity. In both approaches, this scheme can be rendered robust to angular misalignment with adequate engineering solutions.

Furthermore, in the current setup, the nonlinear crystals are not temperature stabilized. It is possible that once engineering constraints, such as a large oven to control the temperature of many crystals evenly and stringently, are overcome, this may help to further improve our setup. In this case it is also possible to use periodically-poled materials, such as PPKTP or PPLN, as these give better signal-to-noise ratio from the higher SPDC efficiency from quasi-phasematching.

4. Conclusion

In summary, using a combination of computational simulations and experimental data, we have provided indications that superlattice-based quantum spectroscopy offers enhancements to interferometric sensitivity. Here, for the first time, we develop the theory for a lossy multi-stage nonlinear interferometric system. Our theory simulates the polychromatic SPDC from crystal superlattices in the presence of idler absorption. This advances quantum gas sensing/spectroscopy, showing how the impact of loss upon quantum correlations from larger crystal superlattices is useful. This type of interferometer is not only in the IR spectroscopy applications, demonstrated here, but also in improving the phase sensitivity in nonlinear interferometers [30].

In particular, we show that more sensitive measurements can be carried out by measuring the fringe maximum intensity via increasing the number of constituent crystals in the superlattice. In addition, the crystal superlattice can be operated with measurement of its visibility, just not at low idler absorber concentrations. This undoubtedly suggests the design of a versatile and highly sensitive superlattice-based Mach-Zehnder interferometric gas sensor. This high interferometric sensitivity can be optimized by adjusting (via simple insertion or removal) the number of constituent crystals.

Optics EXPRESS

While this work solely shows how versatile and sensitive gas spectrometers can be achieved, we believe that our superlattice-based approach offers a compelling path towards further enhancements in quantum metrology and imaging using nonlinear interferometers using correlated photons. A future direction might be compact and robust superlattice-based cavities (i.e., placing superlattices in a Fabry-Perot cavity), which would increase both the idler interaction lengths and effective 'number' of nonlinear elements. This possibility demands the theoretical analysis presented herein.

Funding. Agency for Science, Technology and Research (21709, A2084c0178).

Acknowledgments. Z.S.D.T., A.V.P., and L. A. K. acknowledge the support of from Agency for Science, Technology and Research (A*STAR) via grant funding no. 21709 and AME YIRG 2021 grant funding no. A2084c0178. This work was also supported by the A*STAR Computational Resource Centre through the use of its high-performance computing facilities.

Disclosures. The authors declare no conflicts of interest.

Data availability. Data underlying the results presented in this paper are not publicly available at this time but may be obtained from the authors upon reasonable request.

Supplemental document. See Supplement 1 for supporting content.

References

1. K. E. Dorfman, S. Asban, B. Gu, and S. Mukamel, "Hong-Ou-Mandel interferometry and spectroscopy using entangled photons," Commun. Phys. **4**(1), 49 (2021).
2. D. A. Kalashnikov, E. V. Melik-Gaykazyan, A. A. Kalachev, Y. F. Yu, A. I. Kuznetsov, and L. A. Krivitsky, "Quantum interference in the presence of a resonant medium," Sci. Rep. **7**(1), 11444 (2017).
3. S. Mukamel, M. Freyberger, and W. Schleich, *et al.*, Roadmap on quantum light spectroscopy," J. Phys. B: At., Mol. Opt. Phys. **53**(7), 072002 (2020).
4. A. Paterova, H. Yang, C. An, D. Kalashnikov, and L. Krivitsky, "Measurement of infrared optical constants with visible photons," New J. Phys. **20**(4), 043015 (2018).
5. A. Paterova, S. Lung, D. A. Kalashnikov, and L. A. Krivitsky, "Nonlinear infrared spectroscopy free from spectral selection," Sci. Rep. **7**(1), 42608 (2017).
6. D. A. Kalashnikov, A. V. Paterova, S. P. Kulik, and L. A. Krivitsky, "Infrared spectroscopy with visible light," Nat. Photonics **10**(2), 98–101 (2016).
7. D. A. Kalashnikov, Z. Pan, A. I. Kuznetsov, and L. A. Krivitsky, "Quantum Spectroscopy of Plasmonic Nanostructures," Phys. Rev. X **4**(1), 011049 (2014).
8. H. M. Wiseman and K. Mølmer, "Induced coherence with and without induced emission," Phys. Lett. A **270**(5), 245–248 (2000).
9. X. Y. Zou, L. J. Wang, and L. Mandel, "Induced coherence and indistinguishability in optical interference," Phys. Rev. Lett. **67**(3), 318–321 (1991).
10. L. J. Wang, X. Y. Zou, and L. Mandel, "Induced coherence without induced emission," Phys. Rev. A **44**(7), 4614–4622 (1991).
11. B. Yurke, S. L. McCall, and J. R. Klauder, "SU(2) and SU(1,1) interferometers," Phys. Rev. A **33**(6), 4033–4054 (1986).
12. M. V. Chekhova and Z. Y. Ou, "Nonlinear interferometers in quantum optics," Adv. Opt. Photonics **8**(1), 104–155 (2016).
13. C. Couteau, "Spontaneous parametric down-conversion," Contemp. Phys. **59**(3), 291–304 (2018).
14. G. K. Kitaeva and A. N. Penin, "Spontaneous parametric down-conversion," JETP Lett. **82**(6), 350–355 (2005).
15. T. G. Giallorenzi and C. L. Tang, "Quantum Theory of Spontaneous Parametric Scattering of Intense Light," Phys. Rev. **166**(2), 225–233 (1968).
16. D. Klyshko, "Scattering of light in a medium with nonlinear polarizability," Sov. Phys. JETP **28**, 522 (1969).
17. B. Y. Zel'Dovich and D. Klyshko, "Field Statistics in Parametric Luminescence," Soviet Journal of Experimental and Theoretical Physics Letters **9**, 40 (1969).
18. D. Klyshko, "Coherent photon decay in a nonlinear medium," Soviet Journal of Experimental and Theoretical Physics Letters **6**, 23 (1967).
19. G. K. Kitaeva, V. V. Tishkova, and A. N. Penin, "Characterization of nonlinear optical superlattices by means of ω-k spectroscopy," J. Raman Spectrosc. **36**(2), 116–122 (2005).
20. A. V. Paterova and L. A. Krivitsky, "Nonlinear interference in crystal superlattices," Light: Sci. Appl. **9**(1), 82 (2020).
21. D. Y. Korystov, S. P. Kulik, and A. N. Penin, "Rozhdestvenski hooks in two-photon parametric light scattering," JETP Lett. **73**(5), 214–218 (2001).
22. A. A. Voronin and A. M. Zheltikov, "The generalized Sellmeier equation for air," Sci. Rep. **7**(1), 46111 (2017).
23. L. Mandel and E. Wolf, *Optical Coherence and Quantum Optics* (Cambridge University Press, Cambridge, 1995).

Optics EXPRESS

24. I. E. Gordon, L. S. Rothman, and C. Hill, *et al.*, The HITRAN2016 molecular spectroscopic database," J. Quant. Spectrosc. Radiat. Transfer **203**, 3–69 (2017).
25. R. V. Kochanov, I. E. Gordon, L. S. Rothman, P. Wcisło, C. Hill, and J. S. Wilzewski, "HITRAN Application Programming Interface (HAPI): A comprehensive approach to working with spectroscopic data," J. Quant. Spectrosc. Radiat. Transfer **177**, 15–30 (2016).
26. A. V. Burlakov, M. V. Chekhova, D. N. Klyshko, S. P. Kulik, A. N. Penin, Y. H. Shih, and D. V. Strekalov, "Interference effects in spontaneous two-photon parametric scattering from two macroscopic regions," Phys. Rev. A **56**(4), 3214–3225 (1997).
27. V. S. Education, "CO2 Gas Sensor," retrieved https://www.vernier.com/product/co2-gas-sensor/.
28. CO2Meter.com, "NDIR Single Beam CO2 Sensor Module," retrieved https://www.co2meter.com/products/ndir-single-beam-co2-sensor-module.
29. C. Lindner, J. Kunz, S. J. Herr, S. Wolf, J. Kießling, and F. Kühnemann, "Nonlinear interferometer for Fourier-transform mid-infrared gas spectroscopy using near-infrared detection," Opt. Express **29**(3), 4035–4047 (2021).
30. Z. Y. Ou, "Enhancement of the phase-measurement sensitivity beyond the standard quantum limit by a nonlinear interferometer," Phys. Rev. A **85**(2), 023815 (2012).